CrossMark

High Power Laser Science and Engineering, (2021), Vol. 9, e12, 9 pages.
doi:10.1017/hpl.2021.1

HIGH POWER LASER SCIENCE AND ENGINEERING

RESEARCH ARTICLE

Multi-octave-spanning supercontinuum generation through high-energy laser filaments in YAG and ZnSe pumped by a 2.4 μm femtosecond Cr:ZnSe laser

Sang-Hoon Nam[1], Garima C. Nagar[2], Dennis Dempsey[2], Ondřej Novák[3], Bonggu Shim[2], and Kyung-Han Hong[1,4]

[1]*Research Laboratory of Electronics, Massachusetts Institute of Technology (MIT), Cambridge, MA 02139, USA*

[2]*Department of Physics, Applied Physics and Astronomy, Binghamton University, State University of New York, Binghamton, NY 13902, USA*

[3]*HiLASE Centre, Institute of Physics of the Czech Academy of Sciences, 25241 Dolní Břežany, Czech Republic*

[4]*Presently with MIT Lincoln Laboratory, Lexington, MA 02420, USA*

(Received 23 October 2020; revised 19 December 2020; accepted 5 January 2021)

Abstract

We present experimental and numerical investigations of high-energy mid-infrared filamentation with multi-octave-spanning supercontinuum generation (SCG), pumped by a 2.4 μm, 250 fs Cr:ZnSe chirped-pulse laser amplifier. The SCG is demonstrated in both anomalous and normal dispersion regimes with YAG and polycrystalline ZnSe, respectively. The formation of stable and robust single filaments along with the visible-to-mid-infrared SCG is obtained with a pump energy of up to 100 μJ in a 6-mm-long YAG medium. To the best of the authors' knowledge, this is the highest-energy multi-octave-spanning SCG from a laser filament in a solid. On the other hand, the SCG and even-harmonic generation based on random quasi-phase matching (RQPM) are simultaneously observed from the single filaments in a 6-mm-long polycrystalline ZnSe medium with a pump energy of up to 15 μJ. The numerical simulations based on unidirectional pulse propagation equation and RQPM show excellent agreement with the measured multi-octave-spanning SCG and even-harmonic generation. They also reveal the temporal structure of mid-infrared filaments, such as soliton-like self-compression in YAG and pulse broadening in ZnSe.

Keywords: laser filamentation; mid-infrared laser; nonlinear optics; ultrafast optics

1. Introduction

Recent developments of ultrafast, ultrabroadband high-power laser sources operating in the mid-infrared (mid-IR, ~2–15 μm) have been motivated by applications in unexplored wavelength regimes of strong-field physics[1,2] and nonlinear beam propagations[3,4]. Mid-IR laser filamentation has attracted significant attention owing to the capability of multi-octave-spanning supercontinuum generation (SCG)[5-8], the high-energy pulse propagation with wavelength scaled (~λ^2) critical power, and the spectral coverage of molecular fingerprints region[9,10]. Moreover, mid-IR laser pulses are found to be an excellent tool to access the anomalous group-velocity dispersion (GVD) regime[6] for pumping SCG in most dielectric materials, enabling to study soliton-like pulse propagation dynamics in a laser filament, such as self-compression, self-steepening, and the formation of light bullets. In fact, the self-compression of mid-IR laser pulses in a filament has been theoretically and experimentally studied by a few groups[6–8,11].

Femtosecond mid-IR laser filamentation has been demonstrated predominantly using optical parametric amplification (OPA) and optical parametric chirped-pulse amplification (OPCPA) sources[12,13] that rely on near-IR laser technologies as the pump. However, frequency down-conversion such as in OPA/OPCPA has an inherently low conversion efficiency and the OPA/OPCPA architectures naturally bring complexity to the source itself. Therefore, it is very attractive to directly drive laser filamentation using a mid-IR laser that

Correspondence to: K.-H. Hong, Research Laboratory of Electronics, Massachusetts Institute of Technology (MIT), Cambridge, MA 02139, USA. Email: kyunghan@mit.edu

© The Author(s), 2021. Published by Cambridge University Press in association with Chinese Laser Press. This is an Open Access article, distributed under the terms of the Creative Commons Attribution licence (http://creativecommons.org/licenses/by/4.0/), which permits unrestricted re-use, distribution, and reproduction in any medium, provided the original work is properly cited.

Downloaded from https://www.cambridge.org/core. 06 Apr 2021 at 16:37:19, subject to the Cambridge Core terms of use.

is free of OPA/OPCPA. For example, high-energy mega-filamentation at the wavelength of ~10 μm in air, pumped by a terawatt (TW)-class picosecond CO_2 laser, has been reported very recently[4]. Ultrafast mid-IR solid-state lasers based on transition-metal-doped II–VI semiconductors[14] as a host medium are also attracting great attention because they enable the high-power laser development in wavelength range of 1.8–6 μm in relatively simple, compact, and robust laser configurations similar to those of ultrafast near-IR lasers. Cr:ZnSe is representative of the transition-metal-doped II–VI semiconductors. The advantages of Cr:ZnSe lasers include room-temperature operation, broad tuning in the range of 1.9–3.4 μm, and convenient pumping by reliable Er and Tm fiber lasers. Recently femtosecond multi-mJ Cr:ZnSe lasers have been reported[15]. Despite the recent development of all-solid-state mid-IR laser sources, it is still in early stages of combining the advanced mid-IR lasers and strong-field nonlinear optics. So far, only a handful of reports discuss SCG and other nonlinear optics in bulk crystals pumped by advanced mid-IR solid-state lasers[16–18].

It should be noted that a pump pulse energy at sub-μJ to few μJ level[5–8,19] has been used for laser filamentation and SCG in a solid because the multi-filamentation formation and the optical damage of medium are easily induced at high peak intensities and pulse energies. Energy scaling of a laser filament to the ~100 μJ level in a solid can be much more beneficial for various applications in nonlinear optics and spectroscopy.

In this paper, we experimentally and numerically study high-energy, multi-octave-spanning SCG through mid-IR laser filamentation in the nonlinear materials using an ultrafast Cr:ZnSe laser, which delivers 2.4 μm centered, 250 fs long pulses at 1 kHz repetition rate. Mid-IR laser filaments are generated in bulk media in the anomalous and normal dispersion regimes. We have chosen YAG as an anomalous dispersion medium because it has a negative GVD of –149 fs^2/mm at 2.4 μm of pump wavelength. As a normal dispersion medium, we use ZnSe that has a positive GVD of +224 fs^2/mm at pump wavelength. While increasing the input pulse energy, we capture the spectral and spatial profiles of the filaments in crystals, along with its energy dependence. To obtain a more quantitative understanding of the experiments, we carry out numerical simulations by solving the three-dimensional nonlinear pulse propagation based on the unidirectional pulse propagation equation (UPPE)[20,21] and implementing a random quasi-phase matching (RQPM) model[22]. The simulations reveal the additional details of spatiotemporal dynamics of SCG and harmonic generation of mid-IR filaments in nonlinear crystals.

2. Experimental setup and material properties

We use a mid-IR Cr:ZnSe chirped-pulse amplification (CPA) laser (CLPF-CPA, IPG Photonics) for pumping filamentation. The CPA laser consists of a femtosecond mode-locked Cr:ZnS laser oscillator, a Cr:ZnSe regenerative amplifier, and a grating-based stretcher/compressor[23]. The schematic diagram of the laser system is illustrated in Figure 1(a). The Cr:ZnS oscillator and Ho:YLF pump are optically pumped by continuous-wave (CW) Er-doped fiber and Tm-doped fiber lasers, respectively. The Cr:ZnSe regenerative amplifier is pumped by a *Q*-switched Ho:YLF laser. The laser enclosures are purged by industrial nitrogen gas (95% purity). The Cr:ZnSe CPA laser produces 1.2 mJ, 250 fs pulses with a spectral bandwidth of ~100 nm in full-width at half

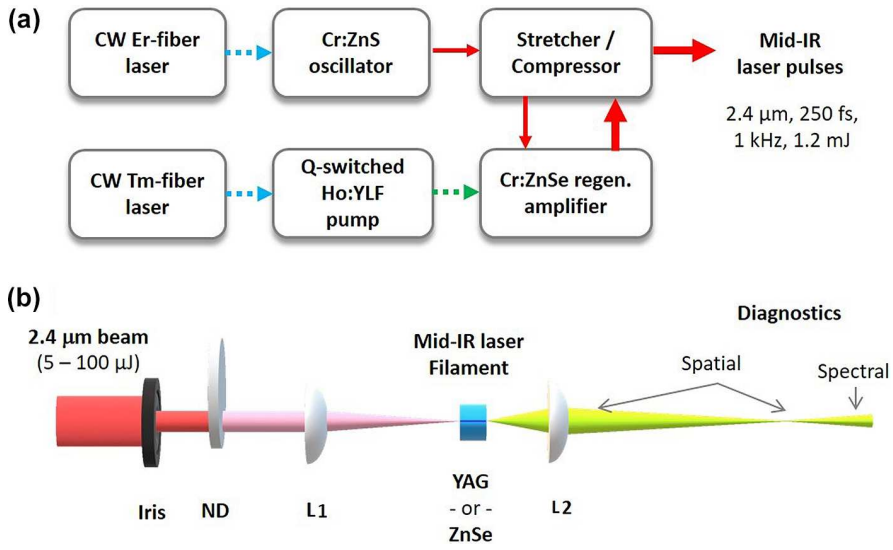

Figure 1. Schematic diagram of experimental setups. (a) Femtosecond Cr:ZnSe CPA laser, composed of mode-locked Cr:ZnS laser oscillator, Cr:ZnSe regenerative amplifier, and stretcher/compressor unit. The dotted lines indicate the pump beam while solid lines, 2.4 μm beams. (b) Setup for laser filamentation in a solid. The arrows for spatial characterization indicate the far-field (left) and near-field (right) images of the laser filament, respectively. The spectral characterization is performed using multiple spectrometers. ND, neutral density filter; L1, $f = 100$ mm CaF_2 lens; L2, $f = 50$ mm CaF_2 lens.

Downloaded from https://www.cambridge.org/core. 06 Apr 2021 at 16:37:19, subject to the Cambridge Core terms of use.

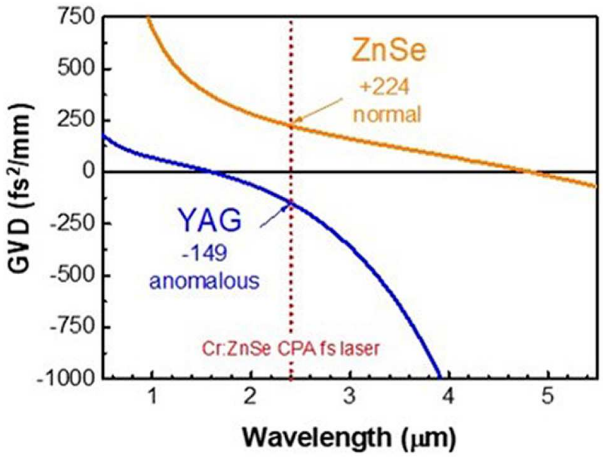

Figure 2. Dispersion curves of YAG and ZnSe versus wavelength. The dotted line shows the pump wavelength of 2.4 μm.

maximum (FWHM) centered at 2.4 μm with a repetition rate of 1 kHz. The further pulse compression is limited by the residual high-order dispersion of the CPA system that can support a transform-limited pulse duration of sub-100 fs. A shot-to-shot pulse energy stability is <5% root mean square (r.m.s.) in general and as good as 2.5% r.m.s. after a sufficient warm-up time (>1 h) and the proper humidity control of laser cavity (<3% of relative humidity). The average output power (~1.2 W) does not drop over an entire day (~8 working hours). The output beam size is ~8 mm × 5 mm in $1/e^2$ beam diameter with some ellipticity of ~0.6.

We utilize a 6-mm-long YAG crystal as filamentation medium in the anomalous dispersion regime. YAG is found to be suitable for mid-IR laser filamentation[5,7,24] owing to the broad transmission range in the mid-IR and high damage threshold. Moderately small, negative GVD value of –149 fs^2/mm at ~2.4 μm is suitable for soliton-like pulse propagation without significant pulse broadening. It has a zero-dispersion wavelength (ZDW, λ_0) at 1.60 μm and the dispersion curve is relatively flat down to the visible range, which enables to extend SCG from the mid-IR to the visible range. For comparison we also choose a 6-mm-long polycrystalline ZnSe having a λ_0 at 4.85 μm and a positive GVD of +224 fs^2/mm at pump wavelength. The GVD curve of both materials is shown in Figure 2[25,26]. The dispersion of ZnSe is relatively flat in the wavelength range from ~1.5 μm to >5.5 μm. Both YAG and ZnSe exhibit a broad transmission range from the visible to the mid-IR spectral range, emerging as attractive nonlinear media in the mid-IR spectral range[27]. The relevant optical parameters, such as energy bandgap (E_g), linear and nonlinear refractive indices (n_0 and n_2), ZDW (λ_0), and critical power (P_{cr}) of YAG and ZnSe at 2.4 μm are listed in Table 1.

As illustrated in Figure 1(b), the 2.4 μm laser beam is focused with an f = 100 mm CaF_2 lens (L1) to the YAG or polycrystalline ZnSe sample. The focusing condition

Table 1. Optical parameters of YAG and ZnSe at 2.4 μm. E_g, energy bandgap[28]; n_0, refractive index at 2.4 μm; n_2, nonlinear index of refraction evaluated at 2.4 μm[29,30]; λ_0, ZDW; P_{cr}, estimated critical power for self-focusing.

Parameters	YAG	ZnSe
E_g (eV)	6.5	2.71
n_0	1.793	2.423
n_2 ($\times 10^{-16}$ cm^2/W)	6.2	22
λ_0 (μm)	1.60	4.85
P_{cr} (MW)	7.7	0.53

and beam size are optimized such that we can maintain a single filament while maximizing the spectral extension of SCG to the mid-IR beyond ~4μm. It turns out that the optimal diameter adjusted with an iris for YAG and ZnSe is 6.0 mm and 2.5 mm, respectively, and the input energy is scanned using a variable neutral-density (ND) filter. The iris also enhances the ellipticity of input beam (~0.6) to better than 0.8 for 6.0 mm of diameter and basically to 1.0 for 2.5 mm of diameter. The YAG or ZnSe sample is placed ~6 mm or ~4 mm, respectively, after the focus in order to avoid the optical damage on/inside the medium while generating a stable filament. The SC beam is collimated using another CaF_2 lens (L2), and then delivered to spectrometers and mid-IR camera for spectral and spatial characterizations. The optical spectra of SC are measured from the visible to mid-IR range using three different spectrometers: fiber-coupled CCS1000 spectrometer (Thorlabs Inc.) for the visible (400–750 nm), fiber-coupled NIR-256-2.5 spectrometer (Ocean Optics Inc.) for the near-IR and short-wavelength IR (870 nm–2.5 μm), and free-space MicroHR monochromator (Horiba Jobin Yvon Inc.) with a mercury cadmium telluride (HgCdTe or MCT) detector for the mid-IR (2–12 μm). The SC spectrum is filtered out using mid-IR band-pass filters (EOC Inc.) with spectral bands of 2.4–4.8 μm and 3–11 μm behind the collimating lens on the way to the diagnostics. The spectra are measured with the entire beam. The collected spectra were corrected to the sensitivity function of the detectors and transmission of the bandpass optical filters. The near-field beam profile of the mid-IR filament is measured with a WinCamD mid-IR camera (DataRay Inc.). The far-field visible profile of the filament is captured on paper using a digital camera. The pulse energy was measured using a wavelength-insensitive pyroelectric power meter (Melles-Griot, 13PEM001) before the input lens (L1 in Figure 1(b)) for the input beam and after the output lens (L2 in Figure 1(b)) for the output beam with SCG.

3. Results and discussion

3.1. Experimental results

Figure 3(a) shows the picture of a typical laser filament inside the 6-mm-long YAG. The visible continuum spectrum

Downloaded from https://www.cambridge.org/core. 06 Apr 2021 at 16:37:19, subject to the Cambridge Core terms of use.

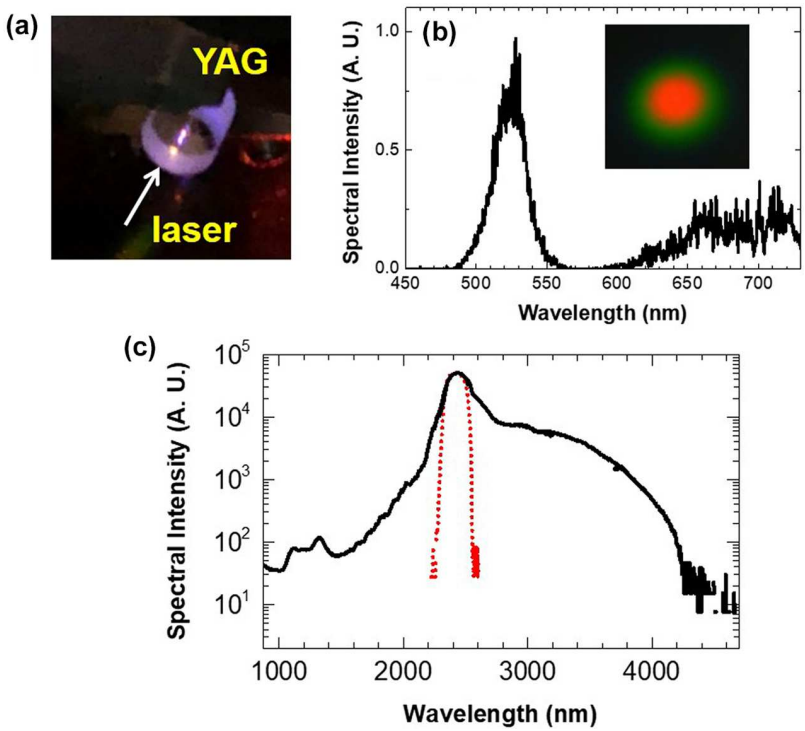

Figure 3. Laser filamentation and SCG in YAG: (a) a laser filament in a 6-mm-long YAG sample; (b) the visible spectrum (linear scale), where the inset is the corresponding far-field beam profile in red and green (true color); and (c) SC spectrum (solid) at 15 μJ, 2.4 μm input (dotted) in logarithmic scale.

(linear scale) from the laser filament with an input pulse energy of ~15 μJ and the corresponding far-field visible beam profile are shown in Figure 3(b), where the spatially dispersed conical emission in green color is due to the effective off-axis three-wave mixing[31]. The third-harmonic generation (THG) at 800 nm must exist, but is not observed due to the spectral gap (750–870 nm) in our measurement. The multi-octave-spanning SC spectra of laser filaments at input pulse energy of 15 μJ are shown as Figure 3(c). A significant spectral broadening to the mid-IR starts at ~10 μJ of input energy while there is no noticeable broadening at ~5 μJ (not shown in the figure). A single laser filament is visibly formed at the pulse energy of 15 μJ. The calculated input peak power at 15 μJ is 60 MW ($7.8P_{cr}$). The SC spectrum covers the mid-IR wavelength to ~4.5 μm although the atmospheric CO_2 absorption at ~4.3 μm hinders the clear cutoff. The visible to mid-IR spectra in Figures 3(b) and 3(c) confirm the near-3-octave-spanning SCG pumped by the Cr:ZnSe laser.

As a comparison, the filamentation and SCG in ZnSe are characterized, as shown in Figure 4. The single filament in yellow color is formed inside ZnSe (Figure 4(a)) as well as the visible far-field profile (Figure 4(b) inset). Owing to the relatively low critical power of ZnSe, the maximum input pulse energy to avoid multi-filament formation is limited to ~15 μJ corresponding to 60 MW or $113P_{cr}$. Although the input beam power is much larger than the threshold for multi-filament formation ($20P_{cr}$–$30P_{cr}$), we believe that relatively small beam sizes for the experiments can inhibit the formation of multi-filaments[32]. The yellow color (~590 nm) turns out to be the fourth-harmonic generation (FHG) of ~2.4 μm pump wavelength due to the polycrystalline nature of ZnSe, which provides a partial phase matching for the second-harmonic generation (SHG) and FHG, as shown as Figures 3(b) and 3(c), owing to RQPM[22]. In addition to the harmonic generation, there is no noticeable spectral broadening to the visible and near-IR ranges unlike in YAG, whereas the octave-spanning mid-IR extension to ~4.8 μm is observed. The steep dispersion curve below ~1.5 μm of wavelength in Figure 2 appears to prevent the SCG from being extended further down to the near-IR and visible ranges. Instead, the SHG (1.2 μm) and FHG peaks are clearly observed. Therefore, we confirm that the nonlinear dynamics of laser filamentation is highly dependent on the dispersion curve of the medium as well as the $\chi^{(2)}$ nonlinearity.

We also scan the input pulse energy to study the energy scaling of laser filaments in these two media. Figures 5(a) and 5(b) present the spectral broadening in YAG and ZnSe versus the input pulse energy in the range of 10–100 μJ, which corresponds to a peak power range of $5.2P_{cr}$–$52P_{cr}$ and $75P_{cr}$–$750P_{cr}$ in YAG and ZnSe at 2.4 μm, respectively. In YAG a noticeable spectral broadening starts to be observed with the input energy of 10 μJ, as shown in Figure 5(a). With further increase of the input energy up to 100 μJ, we observed the gradual extension of SC spectrum to the longer mid-IR part, providing a continuous wavelength

Downloaded from https://www.cambridge.org/core. 06 Apr 2021 at 16:37:19, subject to the Cambridge Core terms of use.

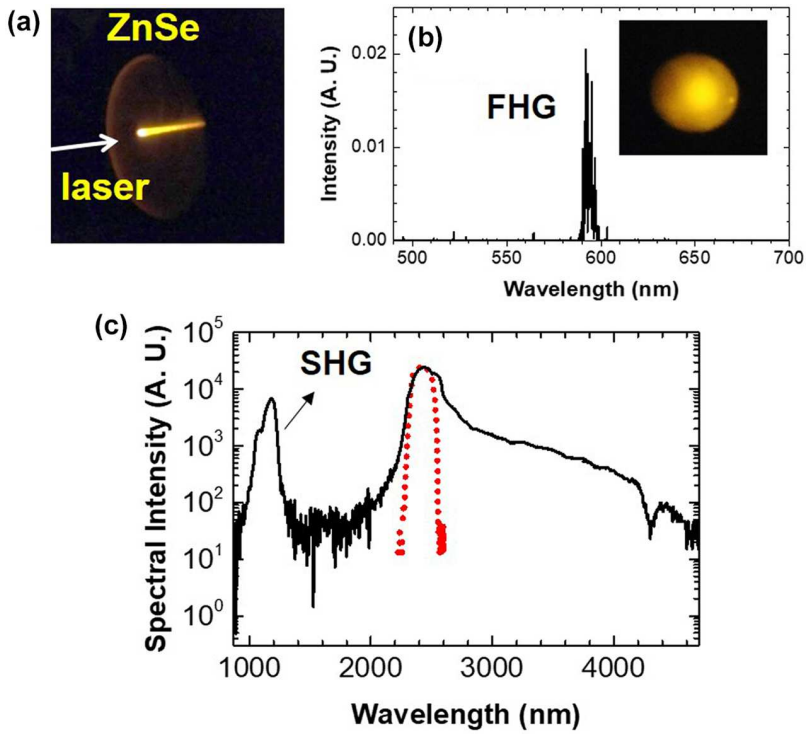

Figure 4. Laser filamentation and SCG in ZnSe: (a) a laser filament in a 6-mm-long polycrystalline ZnSe sample; (b) the visible spectrum (linear scale) showing FHG without SCG, where the inset is the corresponding far-field beam profile in yellow; (c) SC spectrum (solid) at 15 μJ, 2.4 μm input (dashed) in logarithmic scale. The absorption peak at ~4.3 μm is from atmospheric CO_2. The well-defined SHG peak is observed at ~1.2 μm.

coverage to ~4.8 μm. In all cases, the location of the YAG is fixed at 6 mm behind the focus, showing that the YAG is a good candidate with efficient and alignment-insensitive SCG with intense femtosecond mid-IR pulses. The pulse energy loss in the filament is ~25% at 15 μJ and it increases to ~30% at 25 μJ of pump energy. While not measured directly, the energy loss is possibly increased as high as ~40% at 100 μJ of pump energy. Nevertheless, to the best of the authors' knowledge, this is the highest-energy multi-octave-spanning SCG from a laser filament in a solid.

Mid-IR near-field beam profiles of the laser filament were recorded by imaging the output surface of the crystal. The magnification of the images is about two. In all the cases with the input pulse energy of 10–100 μJ in YAG, a stable single laser filament was formed, as verified by the single-peaked good beam profiles in Figure 5(a). The input pulse energy of 100 μJ corresponds to ~160P_{cr}, which is found to be surprisingly high. All these experiments were performed without damaging the crystal at the reported input parameters. With the input energy beyond 100 μJ, not shown here, we still maintained the laser filamentation and SCG, but a noticeable shrinking on the spectra in the mid-IR range was observed. In addition, the formation of multi-filaments was observed, and eventually a permanent damage on the crystal occurred under such a condition. On the other hand, the octave-spanning SC spectra are nearly the same over this pulse energy range (10–100 μJ), indicating the nearly constant peak intensity, which is estimated to ~1.1 × 10^{13} W/cm^2, regardless of the input energy due to the intensity clamping[10] from the formation of laser filament.

It should be noted that during these measurements we have observed that the spectral peaks at 1.1–1.4 μm regularly show up in all the SC spectra at 15–100 μJ of input energy. The SHG in YAG is excluded as a possible origin of these peaks. Instead, they turn out to satisfy the plasma-induced phase matching condition of resonant radiation (RR) of mid-IR laser filaments in YAG, pumped by 2.4 μm laser pulses in anomalous dispersion regime. The origin of RR is similar to the dispersive wave that appears in soliton dynamics in fiber. As the RR is sensitive to the plasma density, the on-axis ($r = 0$) component where the plasma density is the highest is favorable for detection[33]. More detailed dynamics require more experimental and numerical investigations.

We also captured the output SC spectra from ZnSe as presented in Figure 5(b) at various input pulse energies. While the spectral extension to >4.5 μm is easily observed at the pulse energy of 15 μJ (Figure 4(c)) or higher, the mid-IR near-field beam profile indicates that the laser filament starts suffering from irregular ring patterns at 25 μJ of pulse energy, which we believe is attributed to the emergence of multi-filamentation. We eventually observed the optical damage of ZnSe at 50 and 100 μJ. Nevertheless, we demonstrated greater-than-one-octave-spanning SCG in ZnSe with pulse energy of multiple tens of μJ.

Downloaded from https://www.cambridge.org/core. 06 Apr 2021 at 16:37:19, subject to the Cambridge Core terms of use.

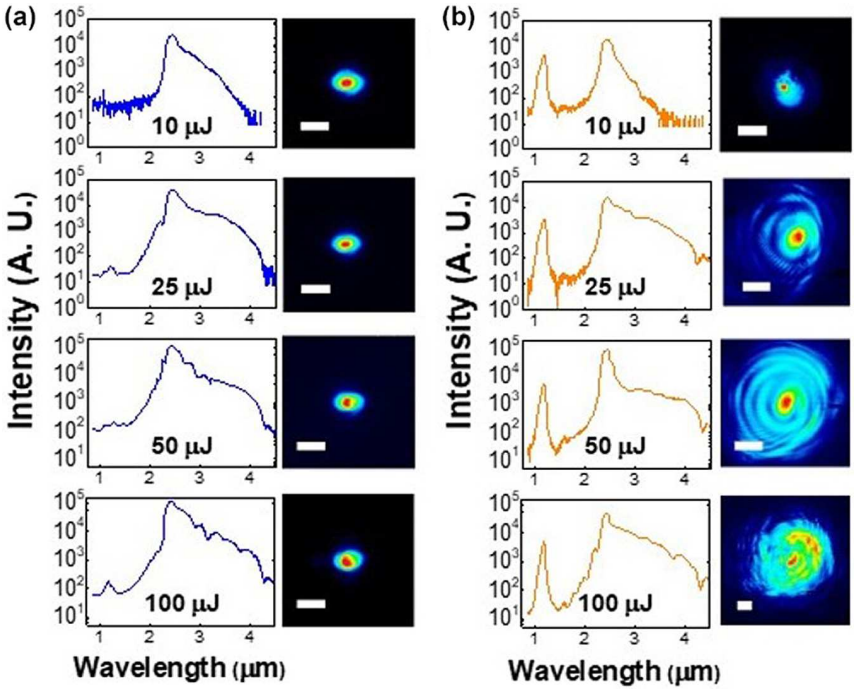

Figure 5. Spectral broadening of incident wavelength of 2.4 μm in a 6-mm-long (a) YAG and (b) ZnSe versus energy and its near-field image. The input pulse energies are 10, 25, 50, and 100 μJ. The logarithmic scale of intensity spectra is used to highlight the fine spectral features. Near-field intensity distributions with the magnification of ~2 at the output surface of the YAG (right column in (a)) and ZnSe (right column in (b)), as measured in the single and multiple filamentation regimes with the variation of input energy. The white scale bars correspond to 0.4 mm in length.

The spectral extension of SCG to the near-IR was very minimal except for the intense SHG peak at 1.2 μm in all the SCG spectra. As discussed earlier along with FHG in Figure 4(b), the RQPM in the polycrystalline structure of ZnSe induces even-harmonic generation[25,34] unlike in YAG. It should be noted that the condition for the single-filament formation in ZnSe was sensitive to the alignment or laser intensity. We had to avoid the generation of a bright blue spot in ZnSe as the input energy was increased. Once we observed the blue spot, we immediately observed the damage. It seems that the sixth-harmonic generation (400 nm, or 3.1 eV) and six photon absorption occur at the same time, inducing the optical damage of ZnSe (2.71 eV of bandgap) before the filament is formed.

3.2. Numerical approach

We performed numerical simulations of pulse propagation through YAG and ZnSe under the conditions similar to the experiments by solving carrier-resolved radially symmetric UPPE[20,21], which is given by

$$\frac{\partial \tilde{E}}{\partial z} = \frac{i}{2k(\omega)}\nabla_{\perp}^2 \tilde{E} + iD\tilde{E} + \frac{i}{2k(\omega)}\frac{\omega^2}{c^2}\frac{\tilde{P}_{\mathrm{NL}}}{\epsilon_0} - \frac{1}{2k(\omega)}\frac{\omega}{c}\frac{\tilde{J}}{\epsilon_0 c} - \frac{\tilde{\alpha}_{\mathrm{NL}}}{2}, \quad (1)$$

where $\tilde{E}$ is the electric field in the spectral domain and z is the propagation distance. The wave vector is $k(\omega) = n(\omega)\omega/c$, where $n(\omega)$ is the linear refractive index, ω is the angular frequency, and c is the speed of light. The dispersion operator is defined as $D = k(\omega) - \omega/\upsilon_g$, where υ_g is the group velocity at the central wavelength 2.4 μm. Here $\tilde{P}_{\mathrm{NL}}$, $\tilde{J}$, and $\tilde{\alpha}_{\mathrm{NL}}$ are the Fourier transform of the nonlinear polarization, free electron effect, and nonlinear absorption due to field ionization, respectively. The nonlinear polarization in the time domain is given by $P_{\mathrm{NL}} = \varepsilon_0 \chi^{(3)} E^3(t)$, where ε_0 is the permittivity of free space and $\chi^{(3)}$ is the third-order nonlinear susceptibility. The free electron current is $\tilde{J} = \left[\left(e^2/m_e\right)(\nu_e + i\omega)/\left(\nu_e^2 + \omega^2\right)\right]\tilde{\rho E}$, where m_e is the electron mass, e is the electron charge, ν_e is the electron collision frequency, and ρ is the free electron density. Absorption due to field ionization is included by $\alpha_{\mathrm{NL}} = \frac{\rho_0 W(I) U}{I} E$, where ρ_0 is the neutral atomic density (7×10^{22} cm^{-3} in YAG and 2.2×10^{22} cm^{-3} in ZnSe), $W(I)$ is the field ionization rate, U = 6.5 eV and 2.71 eV are the bandgap of YAG and ZnSe[5,35], respectively, and I is the intensity of the pulse. Here the terms on the right-hand side of Equation (1) represent diffraction, dispersion, nonlinear polarization, plasma effects, and nonlinear absorption due to field ionization, respectively.

UPPE is coupled with the plasma generation equation, which includes field ionization, collisional ionization, and plasma recombination:

$$\frac{\partial \rho}{\partial t} = W(I)(\rho_0 - \rho) + \frac{\sigma_B I}{U}\rho - \frac{\rho}{\tau_r}, \quad (2)$$

Downloaded from https://www.cambridge.org/core. 06 Apr 2021 at 16:37:19, subject to the Cambridge Core terms of use.

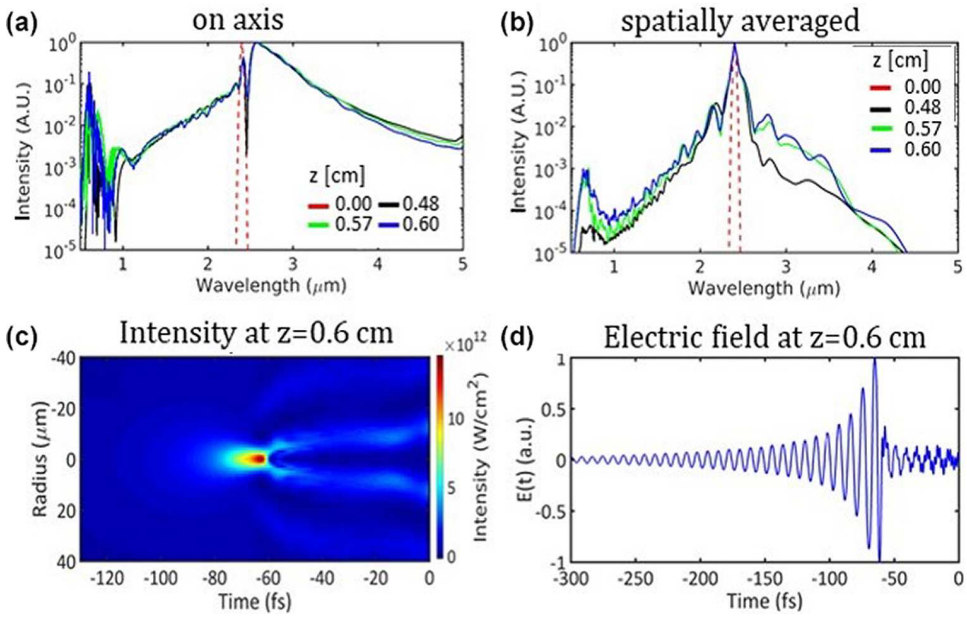

Figure 6. UPPE numerical simulations of SCG in YAG. (a) Simulated on-axis ($r = 0$) spectra and (b) spatially averaged spectra at different propagation distances with the input pulse energy of 50 μJ. (c) Spatiotemporal intensity profile showing self-compression at the end of propagation through YAG and (d) normalized on-axis electric field.

where ρ is the plasma density, σ_B is the inverse bremsstrahlung cross section, and *W(I)* is the field ionization rate, which is multiphoton or tunnel ionization rate depending on the intensity[21]. The avalanche rate follows the Drude model with the collision time of $\tau_c = 3$ fs in solids and the plasma recombination time τ_r in solids is assumed to be 150 fs[6].

The calculated on-axis and spatially averaged spectra from YAG with the input pulse energy of 50 μJ as functions of propagation distance are shown in Figures 6(a) and 6(b), respectively. The main features of experimentally measured SC spectra, such as the mid-IR extension to ~5 μm and visible continuum generation, are well reproduced. The spatiotemporal intensity profile of the mid-IR laser filament from the YAG is shown in Figure 6(c) and its normalized on-axis electric field is shown in Figure 6(d). The self-compression of the main pulse to few-cycle duration due to the anomalous GVD is numerically confirmed.

For the laser filamentation in ZnSe, we implement a numerical model of RQPM. Although polycrystalline ZnSe grains are randomly oriented, nonlinear gain is proportional to $\sqrt{N}$, where N is the number of crystal grains[22]. Following Ref. [36], we add the second-order nonlinearity in the ZnSe simulation, which is given by

$$P_2 = r(z)\epsilon_0 d_2 E^2(t), \tag{3}$$

where $d_2 = 15$ pm/V is the effective second-order nonlinear susceptibility, *r(z)* is a random function between 0 and 1 representing propagation through different grains of the polycrystalline ZnSe. In our simulations, we switch on the random function *r(z)* at every 70 μm step so that it is a constant for 70 μm propagation and is a different constant for the next 70 μm propagation, mimicking the grain size of a polycrystal[36].

The calculated on-axis and spatially averaged spectra from ZnSe with the input energy of 10 μJ as functions of propagation distance are shown in Figures 7(a) and 7(b), respectively. Compared with YAG, spectral broadening is less significant and SHG and FHG are present, which is in good agreement with the experiment. The spatiotemporal intensity profile (Figure 7(c)) and the on-axis electric field (Figure 7(d)) show the multiple pulse splitting in the normal GVD regime.

4. Conclusions

We have experimentally studied the multi-octave-spanning SCG through mid-IR laser filamentation in the nonlinear materials in anomalous and normal dispersion regimes, pumped by a 2.4 μm, 250 fs laser pulses, and numerically investigated the related nonlinear dynamics. Over near-three-octave-spanning SCG spectra were generated from robust and stable high-energy single filaments in YAG which has anomalous dispersion at 2.4 μm. The SCG spectra cover the range of 500 nm–4.5 μm for the input energy range of 10–100 μJ. The result with 100 μJ of input pulse energy demonstrates the highest-energy laser filament in a solid that generates a multi-octave-spanning SC. The SCG of the laser filaments in polycrystalline ZnSe, which is in the normal dispersion regime, not only exhibited greater-than-one-octave-spanning spectra covering the range of 1.5–4.8 μm but also strong even-harmonic generation via RQPM.

Downloaded from https://www.cambridge.org/core. 06 Apr 2021 at 16:37:19, subject to the Cambridge Core terms of use.

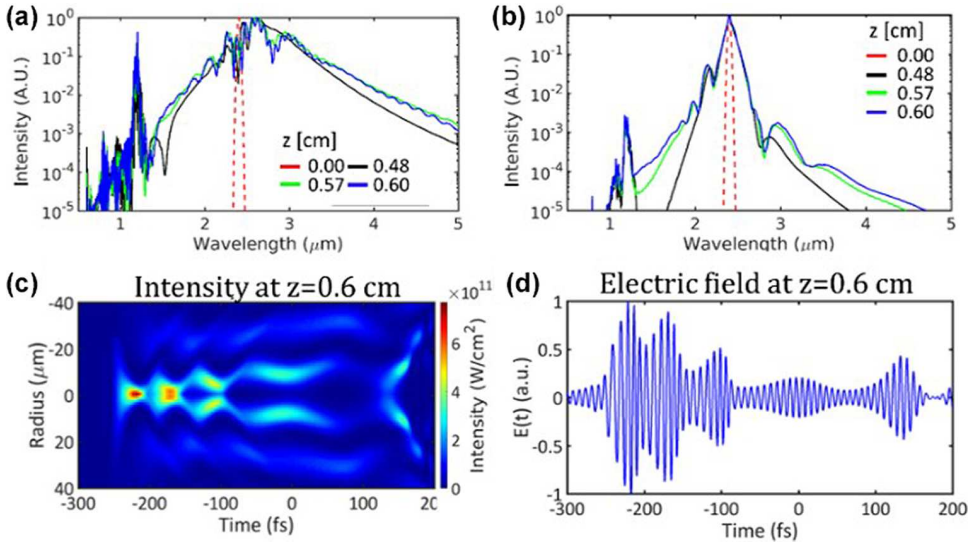

Figure 7. Numerical simulations of SCG in ZnSe. (a) Simulated on-axis ($r = 0$) spectra and (b) spatially averaged spectra with different propagation distances at 10 μJ of input pulse energy. (c) Spatiotemporal intensity profile and (d) normalized on-axis electric field.

The experimental observation agrees well with the numerical simulations based on the UPPE and the RQPM model, which reveal the spatiotemporal dynamics of mid-IR filamentation in a solid. The multi-octave-spanning SCG in YAG and additional even-harmonic generation in ZnSe were qualitatively reproduced with the simulations. The nonlinear dynamics of laser filamentation is found to highly depend on whether it is pumped at anomalous or normal dispersion regime. The mid-IR laser filament in YAG is found to be suitable for seeding a mid-IR OPA system[23] in the wavelength range of 3–10 μm.

Funding

This work was supported by the US DOE accelerator stewardship program (grant number DE-SC0018378), US DOD Office of Navy Research (ONR) DURIP (grant number N00014-17-1-2744), National Science Foundation (NSF) (grant number PHY-1707237), Air Force Office of Scientific Research (AFOSR) (grant number FA9550-18-1-0223), Integrated Electronics Engineering Center (IEEC) of Binghamton University, ERDF and the state budget (grant number CZ.02.1.01/0.0/0.0/15_006/0000674) and MEYS (grant number LO1602, LM2015086) of the Czech Republic, and EU Horizon 2020 (grant number 739573).

Acknowledgments

We thank Dr. S. B. Mirov (UAB and IPG Photonics SETC, USA) for crucial discussions about femtosecond mid-IR lasers as well as Drs. S. Vasilyev and J. Peppers (IPG Photonics SETC) for the design and installation of the Cr:ZnSe regenerative amplifier at MIT. Drs. E. P. Ippen (MIT) and F. X. Kärtner (CFEL-DESY, Germany) are appreciated for the general support with the laboratory infrastructure at MIT.

References

1. T. Popmintchev, M.-C. Chen, D. Popmintchev, P. Arpin, S. Brown, S. Ališauskas, G. Andriukaitis, T. Balčiunas, O. D. Mücke, A. Pugzlys, A. Baltuška, B. Shim, S. E. Schrauth, A. Gaeta, C. Hernández-García, L. Plaja, A. Becker, A. Jaron-Becker, M. M. Murnane, and H. C. Kapteyn, Science **336**, 1287 (2012).
2. S. Ghimire, A. DiChiara, E. Sistrunk, P. Agostini, L. DiMauro, and D. Reis, Nat. Phys. **7**, 138 (2011).
3. P. Panagiotopoulos, P. Whalen, M. Kolesik, and J. V. Moloney, Nat. Photonics **9**, 543 (2015).
4. S. Tochitsky, E. Welch, M. Polyanskiy, I. Pogorelsky, M. Kolesik, P. Panagiotopoulos, E. M. Wright, S. W. Koch, J. V. Moloney, J. Pigeon, and C. Joshi, Nat. Photonics **13**, 41 (2019).
5. F. Silva, D. R. Austin, A. Thai, M. Baudisch, M. Hemmer, D. Faccio, A. Couairon, and J. Biegert, Nat. Commun. **3**, 807 (2012).
6. M. Durand, A. Jarnac, A. Houard, Y. Liu, S. Grabielle, N. Forget, A. Durecu, A. Couairon, and A. Mysyrowicz, Phys. Rev. Lett. **110**, 115003 (2013).
7. M. Hemmer, M. Baudisch, A. Thai, A. Couairon, and J. Biegert, Opt. Express **21**, 28095 (2013).
8. H. Liang, P. Krogen, R. Grynko, O. Novak, C.-L. Chang, G. J. Stein, D. Weerawarne, B. Shim, F. X. Kärtner, and K.-H. Hong, Opt. Lett. **40**, 1069 (2015).
9. A. V. Mitrofanov, A. A. Voronin, D. A. Sidorov-Biryukov, A. Pugžlys, E. A. Stepanov, G. Andriukaitis, T. Flöry, S. Ališauskas, A. B. Fedotov, A. Baltuška, and A. M. Zheltikov, Sci. Rep. **5**, 8368 (2015).
10. H. Liang, D. Weerawarne, P. Krogen, R. Grynko, C.-J. Lai, B. Shim, F. X. Kärtner, and K.-H. Hong, Optica **3**, 678 (2016).
11. S. Qu, G. C. Nagar, W. Li, K. Liu, X. Zou, S. H. Luen, D. Dempsey, K.-H. Hong, Q. J. Wang, Y. Zhang, B. Shim, and H. Liang, Opt. Lett. **45**, 2175 (2020).
12. G. Andriukaitis, T. Balčiūnas, S. Ališauskas, A. Pugžlys, A. Baltuška, T. Popmintchev, M.-C. Chen, M. M. Murnane, and H. C. Kapteyn, Opt. Lett. **36**, 2755 (2011).

Downloaded from https://www.cambridge.org/core. 06 Apr 2021 at 16:37:19, subject to the Cambridge Core terms of use.

13. K.-H. Hong, C.-J. Lai, J. P. Siqueira, P. Krogen, J. Moses, C.-L. Chang, G. J. Stein, L. E. Zapata, and F. X. Kärtner, Opt. Lett. **39**, 3145 (2014).
14. S. B. Mirov, V. V. Fedorov, D. Martyshkin, I. S. Moskalev, M. Mirov, and S. Vasilyev, IEEE J. Sel. Top. Quantum Electron. **21**, 1601719 (2015).
15. X. Ren, L. Mach, Y. Yin, Y. Wang, and Z. Chang, Opt. Lett. **43**, 3381 (2018).
16. Q. Wang, J. Zhang, A. Kessel, N. Nagl, V. Pervak, O. Pronin, and K. F. Mak, Opt. Lett. **44**, 2566 (2019).
17. S. Vasilyev, I. Moskalev, M. Mirov, V. Smolski, S. Mirov, and V. Gapontsev, Opt. Mater. Express **7**, 2636 (2017).
18. G. Vampa, S. Vasilyev, H. Liu, M. Mirov, P. H. Bucksbaum, and D. A. Reis, Opt. Lett. **44**, 259 (2019).
19. A. Choudhuri, G. Chatterjee, J. Zheng, I. Hartl, A. Ruehl, and R. J. D. Miller, Appl. Phys. B **124**, 103 (2018).
20. M. Kolesik and J. V. Moloney, Phys. Rev. E **70**, 036604 (2004).
21. R. I. Grynko, G. C. Nagar, and B. Shim, Phys. Rev. A **98**, 023844 (2018).
22. M. Baudrier-Raybaut, R. Haïdar, P. Kupecek, P. Lemasson, and E. Rosencher, Nature **432**, 374 (2004).
23. S.-H. Nam, V. Fedorov, S. Mirov, and K.-H. Hong, Opt. Express **28**, 32403 (2020).
24. S. Cheng, G. Chatterjee, F. Tellkamp, A. Ruehl, and R. J. Dwayne Miller, Opt. Lett. **43**, 4329 (2018).
25. D. E. Zelmon, D. L. Small, and R. Page, Appl. Opt. **37**, 4933 (1998).
26. D. T. F. Marple, J. Appl. Phys. **35**, 539 (1964).
27. R. Šuminas, G. Tamošauskas, G. Valiulis, V. Jukna, A. Couairon, and A. Dubietis, Appl. Phys. Lett. **110**, 241106 (2017).
28. M. J. Weber, *Handbook of Optical Materials* (CRC Press, Boca Raton, 2003).
29. J. Darginavičius, D. Majus, V. Jukna, N. Garejev, G. Valiulis, A. Couairon, and A. Dubietis, Opt. Express **21**, 25210 (2013).
30. M. Sheik-Bahae, D. C. Hutchings, D. J. Hagan, and E. W. Van Stryland, IEEE J. Quantum Electron. **27**, 1296 (1991).
31. M. Kolesik and J. V. Moloney, Opt. Express **16**, 2971 (2008).
32. R. I. Grynko, D. L. Weerawarne, X. Gao, H. Liang, H. J. Meyer, K.-H. Hong, A. L. Gaeta, and B. Shim, Opt. Lett. **41**, 4064 (2016).
33. S.-H. Nam, G. C. Nagar, D. Dempsey, O. Novak, B. Shim, and K.-H. Hong, in *Frontiers in Optics and Laser Science* (2019), paper JW4A.111.
34. X. Vidal and J. Martoreli, Phys. Rev. Lett. **97**, 013902 (2006).
35. T. D. Krauss and F. W. Wise, Appl. Phys. Lett. **65**, 1739 (1994).
36. K. Werner, M. G. Hastings, A. Schweinsberg, B. L. Wilmer, D. Austin, C. M. Wolfe, M. Kolesik, T. R. Ensley, L. Vanderhoef, A. Valenzuela, and E. Chowdhury, Opt. Express **27**, 2867 (2019).

Downloaded from https://www.cambridge.org/core. 06 Apr 2021 at 16:37:19, subject to the Cambridge Core terms of use.